Numerical Investigation of Acoustic Liners Experimental Techniques using a Lattice-Boltzmann Solver

Schroeder, Lucas; Spillere, André M. N.; Bonomo, Lucas A.; da Silva, Andrey R.; Cordioli, Júlio A.; Avallone, F.

DOI
10.2514/6.2021-2144

Publication date
2021

Document Version
Final published version

Published in
AIAA AVIATION 2021 FORUM

AIAA AVIATION Forum
August 2-6, 2021, VIRTUAL EVENT
AIAA AVIATION 2021 FORUM

10.2514/6.2021-2144

Numerical Investigation of Acoustic Liners Experimental Techniques using a Lattice-Boltzmann Solver

Lucas Schroeder*, André M. N. Spillere†, Lucas A. Bonomo‡, Andrey R. da Silva§ and Júlio A. Cordioli¶
Federal University of Santa Catarina, Florianópolis, 88040-900, Brazil

Francesco Avallone‖
Delft University of Technology, 2629 HS Delft, The Netherlands

The physics behind acoustic liners attenuation in the presence of flow and high sound pressure level is still a matter of debate. Similarly, discrepancies between experimental results and numerical data have been linked to the boundary conditions used to model the liner and boundary layer effects, and the reasons behind these discrepancies are still not clear. In this sense, to avoid the limitations of the boundary condition approach, fully resolved high fidelity computation models of the liner and its dissipation mechanisms may be an important tool to improve understanding. The present study carries out a numerical analysis using a code based on the Lattice-Boltzmann method, and special focus is given on replicating the results from different experimental techniques used to evaluate the liner impedance: the in-situ method and an impedance eduction method based on the mode-matching technique. The study is conducted with a model including a single degree of freedom liner with multiple cavities based on a real geometry. The model considers high sound pressure level, grazing plane acoustic waves without flow in order to replicate the experimental setup. A mesh convergence analysis is performed, and the liner impedance obtained numerically is compared with experimental results from the in-situ method and the impedance eduction technique. The numerical pressure and velocity fields are also analyzed in detail to better understand the damping mechanisms and physics involved.

I. Introduction

STRINGENT noise regulations are an important part of the certification process of an aircraft. In order to meet these criteria, acoustic liners play a major role in the noise reduction of turbofan engines, particularly at the blade passing frequency tones. These noise absorbing materials are generally composed of a perforated facesheet, honeycomb core and rigid backplate. Despite its simplistic construction, their characterization in the presence of grazing flow and high sound pressure levels, as typically found in flight conditions, remains a complex task. Whereas experimental techniques can be used to assess their acoustic impedance under realistic conditions, numerical investigations can provide valuable insights into flow-acoustic interactions and non-linear behavior, and consequently lead to improved liner designs.

Since simulations of the typical liner geometry may be computationally demanding, simplified geometries are often used in preliminary studies in order to shed some light into the fundamental mechanisms of acoustic dissipation, for example by considering a two-dimensional Helmholtz resonator [1–4]. However, Tam et al. [5] observed that the vortex shedding phenomenon at the resonator opening may differ in three-dimensional simulations. An additional limitation may arise from simulations of a single liner cavity, for example an hexagonal geometry with multiple orifice at the facesheet [6, 7], which may be insufficient to capture the complex flow and acoustic interactions between adjacent cells.

In general, numerical simulations of acoustic liners are compared to experimental results obtained with normal incidence impedance tubes [2, 5]. On the other hand, when performing simulations with grazing flow, it is almost inevitable to compare with data from dedicated liner test rigs using either in-situ [8] or impedance eduction techniques [9]. For instance, Tam et al. [10] reproduced numerically the NASA Langley Grazing Flow Impedance Tube in the

*MSc Student, Department of Mechanical Engineering, lucas.schroeder@lva.ufsc.br, Non AIAA Member
†PhD Student, Department of Mechanical Engineering, andre.spillere@lva.ufsc.br, Non AIAA Member
‡PhD Student, Department of Mechanical Engineering, lucas.bonomo@lva.ufsc.br, Non AIAA Member
§Associate Professor, Department of Mechanical Engineering, andrey.rs@ufsc.br, AIAA Member
¶Associate Professor, Department of Mechanical Engineering, julio.cordioli@ufsc.br, AIAA Member
‖Assistant Professor, Department of Aerodynamic, Wind Energy and Propulsion, f.avallone@tudelft.nl, AIAA Member

presence of eight slit resonators with grazing flow, but a mismatch between experimental and numerical acoustic fields could be observed, especially close to the slit resonance frequency. More recently, Zhang and Bodony [6] compared the numerical in-situ impedance of a single orifice hexagonal cavity with the educed impedance of a typical liner sample. The considerable differences between numerical and experimental setups may create an additional challenge to the validation of simulation results. Correspondingly, eduction methods usually present high variability in the results due to experimental errors [11], which can be greatly reduced in the numerical domain to produce comparisons between different impedance measurement techniques.

In order to gain confidence in the numerical simulation of acoustic liners, we investigate the acoustic behavior of an acoustic liner in a typical experimental facility, such as the Liner Test Rig located at the Federal University of Santa Catarina (UFSC). We consider both in-situ and impedance eduction techniques, which are based on the work of Dean [8] and Spillere et al. [12], respectively. Whereas in-situ technique gives the *local* impedance of a single cell, impedance eduction methods return the *average* impedance of liner samples. Therefore, this study can also be seen as a cross-validation of both techniques. Results are compared with the experimentally educed impedance of a typical low-porosity single-degree-of-freedom liner sample, as well as the impedance measured with in-situ technique, as published in Spillere et al. [13]. As a means to save computational resources, the total liner length is reduced, but the relevant design parameters i.e. facesheet geometry and cavity height are kept the same. Both linear and non-linear regimes i.e. low and high incident sound pressure levels for the no flow case are initially considered. Ultimately, this study is a validation step of numerical impedance determination methods, which shall be used in more advanced configurations, such as in the presence of grazing flow. In this way, questions like the apparent liner impedance dependence on the flow direction relative to the acoustic source [12, 14] may be answered in the future.

Instead of solving the Navier-Stokes equations with traditional techniques such as the direct numerical simulation (DNS) or large eddy simulation (LES), we consider the Boltzmann equation which describes the particles dynamics at a mesoscopic scale. It is possible to show that the weakly compressible Navier-Stokes equations and the Boltzmann equation are equivalent [15]. The discrete version of the Boltzmann equation is known as the lattice-Boltzmann method, and in the present work it is solved using the commercial software package 3DS Simulia PowerFlow 6-2019. Previous related works using this numerical tool include simulation of a multi-cavity acoustic liner in a normal incidence impedance tube [16] and single-cavity acoustic liner grazed by turbulent flow [7].

This paper is organized as follows. Section II contains a description of the numerical model, including the governing equations and numerical solver. Section III describes the experimental techniques for liner characterization that shall be applied in the numerical model. Section IV show two model verification methods used to assure the model concept is correctly implemented, while Section V presents a validation of the numerically obtained impedances by comparing with in-situ and experimentally educed impedances of a typical acoustic liner sample for the case with no flow.

II. Numerical Model

A. Governing Equations

1. Lattice-Boltzmann Method

The Boltzmann equation models the fluid in a mesoscopic scale based on the statistical description of the particle motion, i.e. the probability of finding a particle at a certain location with a certain velocity at a certain time [17]. The fundamental variable is the distribution function $f(\boldsymbol{x}, \boldsymbol{\xi}, t)$, that is the probability density of particles with the velocity set $\boldsymbol{\xi} = (\xi_x, \xi_y, \xi_z)$ at the position $\boldsymbol{x} = (x, y, z)$ in the instant t, and it has units of $[f] = \mathrm{kg} \cdot \frac{1}{\mathrm{m}^3} \cdot \frac{1}{\left(\frac{\mathrm{m}}{\mathrm{s}}\right)^3} = \frac{\mathrm{kg\,s}^3}{\mathrm{m}^6}$. Denoting $\Omega(f) = \frac{df}{df}$ for the total differential, the Boltzmann equation describes the evolution of the distribution function in time, where $\Omega(f)$ is called the collision operator:

$$\frac{\partial f}{\partial t} + \xi_\beta \frac{\partial f}{\partial x_\beta} + \frac{d\xi_\beta}{dt} \frac{\partial f}{\partial \xi_\beta} = \Omega(f). \tag{1}$$

f is the solution of the Boltzmann equation and is expanded in a series of Hermite polynomials [18]. These constitute an orthogonal basis, which is particularly suited to describe a flow in the kinetic space. Indeed, the first four coefficients, from 0^{th} to 3^{rd} order, of the expansion of the Maxwellian distribution function $f^{(0)}$ at equilibrium are algebraically related to the moments of macroscopic flow, say mass, momentum, energy/momentum fluxes, and heat fluxes.

An interesting property of a Hermite expansion is that the series can be truncated at a given order without altering the low-order coefficients; therefore an expansion of f truncated at the order $N > 3$ provides a unique representation of the macroscopic hydrodynamic status of a fluid. Macroscopic quantities can be derived from the distribution function using its moments, which is calculated by integrating the distribution function f in the whole velocity space weighted by some power of the velocity space ξ. For instance, the density ρ and momentum $\rho\boldsymbol{u}$ are calculated using

$$\rho(\boldsymbol{x},t) = \int f(\boldsymbol{x},\xi,t)d^3\xi \quad \text{and} \quad \rho(\boldsymbol{x},t)\boldsymbol{u}(\boldsymbol{x},t) = \int \boldsymbol{\xi} f(\boldsymbol{x},\xi,t)d^3\xi. \tag{2}$$

Solving the Boltzmann Equation would require solving for the seven-dimensional space defined in the distribution function. Instead, the Hermite series expansion can be used to derive a small set of discrete velocities in the 3D space that still allows to recover the macroscopic behavior of the fluid [17]. The code uses a symmetric discretization of the velocity space according to the D3Q19 model. The magnitude and direction of each particle velocity vector is such that the distribution function can be advected from one node of a computational lattice to the neighboring points during a single time step, independently of the local grid refinement. When discretized for an equidistant lattice, considering the space increment $\xi_i\Delta t$, a modified form of the Boltzmann Equation is obtained as

$$f_i(\boldsymbol{x} + \boldsymbol{\xi}_i\Delta t, t + \Delta t) = f_i(\boldsymbol{x},t) + \Delta t\Omega_i(\boldsymbol{x},t), \tag{3}$$

where f_i and $\boldsymbol{\xi}_i$ are the particle distribution function and discrete particle velocity, respectively, in i-th direction. Equation 3 is known as Lattice Boltzmann Equation. Ω_i is the discrete form of the collision term Ω, the well-known Bhatnagar-Gross-Krook (BGK) operator [19], and, according to Chen et al. [20] it is implemented by

$$\Omega_i(\boldsymbol{x},t) = -\frac{1}{\tau}\left(f_i(\boldsymbol{x},t) - f_i^{\text{eq}}(\boldsymbol{x},t)\right). \tag{4}$$

It is possible to show that the BGK collision operator leads to a exponential decay $(f_i - f_i^{\text{eq}}) \propto \exp(-t/\tau)$ if f_i^{eq} is constant [17]. That is why τ is called the relaxation time. The equilibrium distribution function f_i^{eq} approximated up to third order is given by [20]

$$f_i^{\text{eq}} = \rho w_i\left(1 + \frac{\boldsymbol{\xi}_i\cdot\boldsymbol{u}}{T_l} + \frac{(\boldsymbol{\xi}_i\cdot\boldsymbol{u})^2}{2T_l^2} - \frac{|\boldsymbol{u}|^2}{2T_l} + \frac{(\boldsymbol{\xi}_i\cdot\boldsymbol{u})^3}{6T_l^3} - \frac{(\boldsymbol{\xi}_i\cdot\boldsymbol{u})}{2T_l^2}\boldsymbol{u}^2\right). \tag{5}$$

The weighting factors w_i, according to the D3Q19 scheme, are equal to $1/3$ for the rest particles, $1/18$ for the 12 bi-diagonal directions and $1/36$ for the 6 coordinate directions. The lattice temperature T_l is set to $1/3$ for isothermal flows, leading to a constant lattice sound speed of $C_s = 1/\sqrt{3}$ in lattice units. As a consequence, the equation of state can be expressed as $p = \rho C_s$. The relaxation time τ is related to the kinematic viscosity ν by

$$\tau = \frac{\nu}{T_l} + \frac{\Delta t}{2}, \tag{6}$$

and its value is limited to a maximum in order to enhance code stability [21].

The lattice-Boltzmann algorithm consists of a sequence of substeps that make up a timestep. After the initialization, the macroscopic moments $\rho(\boldsymbol{x},t)$ and $\boldsymbol{u}(\boldsymbol{x},t)$ are obtained from the moments of f_i in Equation 2 to find the equilibrium distribution function with Equation 5, then Equation 3 is used to compute the new distribution function. This substep is called collision or relaxation, and the distribution function after collisions is denoted by f_i^*. It is then propagated to the neighboring nodes in the streaming substep using $f_i(\boldsymbol{x} + \xi_i\Delta t, t + \Delta t) = f_i^*(\boldsymbol{x},t)$. After this, the time variable is increased to $t + \Delta t$ and the process repeats for the next timestep until the end.

Each cubic volume of the mesh is called Voxel. The grid refinement is defined by creating regions of local variable grid resolution (VRs), which scale between each other by a factor of 2. Calculations in the VR transitions boundaries are done by a grid refinement algorithm described in Ref. [22], which was developed in order to satisfy conservation laws.

2. Turbulence Model

For high Reynolds number flows it is not computationally feasible to account for every spatial and temporal scale. For this reason, the code model the smaller scales behavior using the VLES approach, which is very well suited for LB method. In this approach, large scales are directly simulated, whereas the contribution of unsolved scales are accounted by means of an eddy viscosity model. PowerFLOW modifies the relaxation time in the collision operator by considering

the time scales related to the turbulent motion and to the strain rate and rotation of the resolved flow field. Moreover, the amount of turbulent kinetic energy is used to define the equilibrium state of the gas. The molecular relaxation time is replaced by an effective turbulent relaxation time, including the eddy viscosity effects [23]. The turbulence model used is a modification of the two-equation renormalization group (RNG) $k-\epsilon$ [21, 24]. The corrected relaxation time scale is then

$$\tau_{\text{eff}} = \tau + C_\mu \frac{k^2/\epsilon}{(1+\tilde{\eta}^2)^{\frac{1}{2}}}, \tag{7}$$

where C_μ is a turbulence model constant and $\tilde{\eta}$ is a combination of a local strain parameter, local vorticity and local helicity [23]. These values scale the contribution of the eddy viscosity in τ_{eff}, allowing structures which can be resolved by the grid to be developed and persist without numerical damping. Differently for NS-based methods, the RNG model is used to dynamically re-calibrate the Boltzmann model to the characteristic time scales of a turbulent flow motion. Hence, no Reynolds stresses are explicitly added to the governing equations, and those are an implicit consequence of the chaotic exchange of momentum driven by the turbulent flow with characteristic times smaller than the slowly-varying turbulent flow. The turbulence model equations are solved in the same grid as the LBM, but with a modified Lax-Wendroff explicit second order finite difference scheme [21].

3. Wall Model

High Reynolds number flows usually have high velocity gradients at the boundary layer in the wall normal direction. The nature of the computational grid used in lattice-Boltzmann simulations does not allow for the traditional grid stretching technique and a good approach is to incorporate a wall model. PowerFLOW uses the Law of the Wall, a universal nongeometry-dependent velocity profile adjusted with empirical data [24] to model the effects of the wall in the fluid. This model allows to use a relatively simple set of equations to calculate the the friction velocity u_τ as well as the turbulent quantities at the first voxel near the wall.

To achieve the desired behavior, the general wall model implemented is pressure-gradient dependent. The code computes the flow velocity in the first cell above the surface, where the velocity is usually not zero. Analyzing the non-dimensional wall velocity $y^+ \equiv y u_\tau/\nu$, where $u_\tau = \sqrt{\tau_w/\rho}$ is the friction velocity, the code determines whether the Law of the Wall holds at this position. If so, the velocity profile is assumed to follow a logarithmic profile given by Equation 8 and the shear stress at the wall can be assumed equal to the one in this position.

$$\frac{u}{u_\tau} = \frac{1}{\kappa}\ln\left(y^+\right) + B \quad (30 < y^+ \lessapprox 500), \tag{8}$$

where the non-dimensional constants κ and B had been found experimentally to be 0.41 and 5.0 respectively. The local skin friction coefficient C_f is related to the wall friction τ_w via the friction velocity u_τ

$$\tau_w \equiv \rho u_\tau^2 = \frac{1}{2} C_f \rho u^2. \tag{9}$$

These two equations can be solved together to determine C_f and u_τ. If the dimensionless distance $y^+ \equiv y u_\tau/\nu < 30$ the velocity profile have to be adjusted for the buffer and viscous sub-layer regions accounting for the eddy viscosity $\nu_t = C_\mu k^2/\epsilon$.

B. Geometry and Simulation Domain

For this study, it was chosen a liner geometry that has already been tested in previous works at UFSC by Spillere et al. [25]. The liner consists of a rigid facesheet of thickness $\tau = 0.80$ mm, eleven square cavities of side $l = 9.20$ mm, height $h = 38.50$ mm and wall thickness of $w = 0.80$ mm, resulting in a streamwise liner length of 110 mm. There are 6 orifices per cavity, each with a diameter of $d = 1.0$ mm, resulting in a porosity of $\sigma = 4.8$ %. The rigid backplate does not allow for the neighboring cells to communicate. The actual geometry of the liner used in the numerical simulations is shown in Fig. 1.

The UFSC liner test rig has a rectangular cross section that is 40 mm high and 100 mm wide. However, for the simulation, the liner sits inside a duct 40 mm high and 10 mm wide, with a periodic boundary condition in the width direction to reduce computational cost. As shown in Fig. 2, no-slip boundary condition is applied at walls near the liner, but in the opposite (bottom) wall and in the sponge region, the walls have a free-slip boundary condition. The inlet is set to zero free stream velocity and the outlet is set to constant pressure. Sponge layers are defined near the inlet and outlet

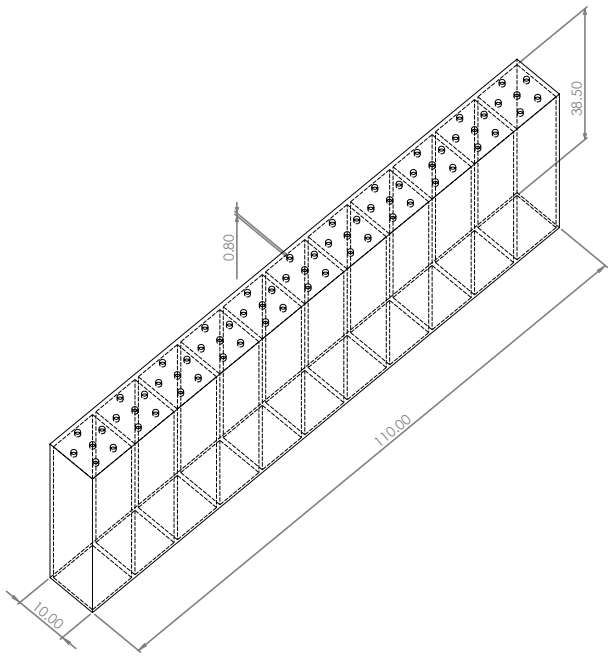

Fig. 1 Liner row geometry, eleven cavities in total.

of the duct to prevent any inward reflection of the acoustic waves. The buffer zone between the useful section and the sponge layers are defined by an exponential increase of the damping parameter ν/T, which starts at a minimum of 0.005 at the useful simulation volume, up to 0.5 in the sponge layer. The acoustic source is simulated by superimposing an harmonic acoustic wave to the simulation volume and running the simulation to let the wave propagate. Acoustic waves at frequencies $f_1 = 800\,\text{Hz}$, $f_2 = 1400\,\text{Hz}$ and $f_3 = 2000\,\text{Hz}$ were simulated with amplitudes of 130 dB and 150 dB each, where the Sound Pressure Level is relative to 20 µPa.

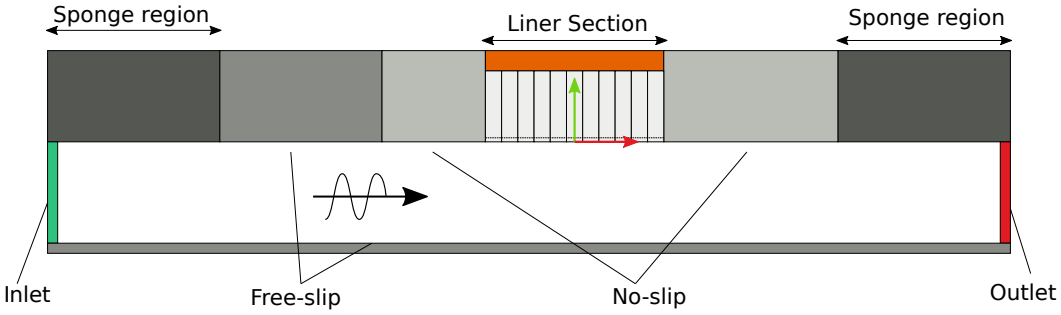

Fig. 2 Numerical domain and boundary conditions.

In order to access the grid resolution impact on the results, two levels of resolution were simulated, 12.8 and 25.6 voxels/mm, that leads to approximately 8 and 16 voxels across the orifice height, respectively. Fig. 3 shows the coarse grid configuration, and the different VRs can be seen in the streamwise cross section of the duct and liner assembly.

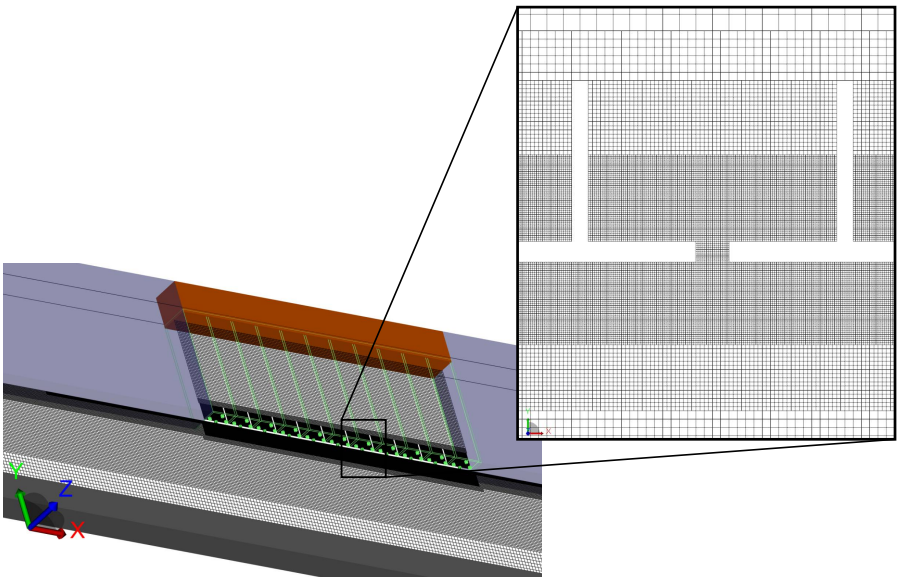

Fig. 3 Computational grid near the orifice.

III. Impedance Measurement Techniques

A. In-Situ Technique

One of the earliest impedance measurement techniques for acoustic liners was developed by Dean [8] and consists of acquiring acoustic pressure at the facesheet and backplate. In frequency domain, these are related by $H_{\text{pair}} \equiv (P_{\text{f}}/P_{\text{b}})\exp(\text{i}\phi)$, where P_{f} and P_{b} are the pressure amplitudes at the facesheet and backplate, respectively, and ϕ is their phase difference, as schematically shown in Fig. 4a. From that, it is possible to show that liner normalized impedance Z is given by

$$Z = -\text{i}H_{\text{pair}}\frac{1}{\sin(kh)}, \tag{10}$$

where $\text{i} = \sqrt{-1}$, $k = \omega/c_0$ is the free-field wavenumber and h is the cavity height. In practice, this impedance must be corrected to account for the presence of small pressure transducers which are inserted into the honeycomb cavity [26]. However, numerical simulations do not suffer from this limitation, and therefore no corrections need to be made. Furthermore, the pressure measurement usually is obtained by small area pressure transducer, which can be replicated in the simulation and compared with the pressure average over the cavity facesheet and backplate areas.

B. Impedance Eduction Method

Impedance eduction methods have received growing attention over the past decades (e.g. [26, 27]). These methods avoid instrumentation of the liner sample, which could potentially affect its own impedance, and instead focus on the instrumentation of test rigs, with flush-mounted microphones at the duct walls the most popular choice (e.g. [12, 26]). From that, governing equations of the acoustic propagation are necessary in order to relate measurements with a numerical model of the acoustic field. In this case, the liner sample is treated as an impedance boundary condition, and optimization routines can be employed to *educe* the liner impedance that best fits experimental and numerical results. Alternative methods, such as direct extraction of axial wavenumbers in a lined section by means of Prony's method [14, 28], are not considered in this work.

We consider a mode-matching model to compute the acoustic field, details of which can be found in Spillere et al. [12], and summarized as follows. The test rig is divided into three segments, as schematically shown in Fig. 4b. In the absence of flow, the Helmholtz equation is solved at each duct segment with appropriate boundary conditions (rigid or lined) using a pseudospectral method, yielding the axial wavenumbers and mode shapes. The modal amplitudes are determined by matching solutions at each interface assuming continuity of mass and momentum, which is equivalent to

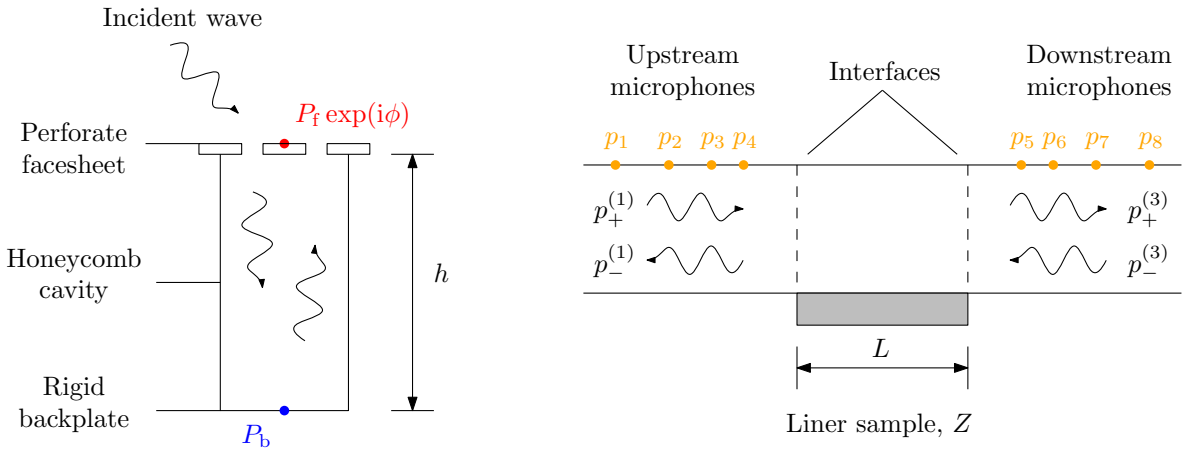

(a) In-Situ Technique (b) Impedance Eduction Technique

Fig. 4 Schematic view of in-situ and impedance eduction techniques.

continuity of pressure and axial velocity in this case. Inputs to the model are the plane-wave amplitudes at upstream and downstream sections propagating towards the liner, which are computed using an over-determined plane wave decomposition method. The initial guess for Z is provided by a semi-empirical liner impedance model. The difference between experimental p_q^{exp} and numerical p_q^{num} acoustic fields at the q-th microphone is used to compute the cost function,

$$\mathcal{F}(Z) = \sum_{q=1}^{8} \left| \frac{p_q^{\text{exp}} - p_q^{\text{num}}(Z)}{p_q^{\text{exp}}} \right|. \tag{11}$$

which can be minimized using the Levenberg–Marquadt algorithm [29, 30]

IV. Model Verification

A. Mesh Convergence

Lattice-Boltzmann schemes tends to asymptotic solutions when the computational grid is infinitely small [17], so we may evaluate mesh convergence to verify the errors introduced by domain discretization. Table 1 shows the difference in normalized impedance obtained with different grid resolutions. For increasing frequencies and sound pressure levels, the computational grid tends to have a greater influence, since there are higher pressure and velocity gradients. However, all the differences are smaller than 15% of the air's impedance.

Another important evidence of the effectiveness of the numerical grid resolution can be seen in Fig. 5, where the finer mesh performed better in reproducing the experimental results. This give us confidence that the grid is good enough to capture the physics of all simulated scenarios.

Table 1 Difference in reactance and resistance obtained from the numerical simulation using the in-situ method with medium and fine grid resolutions $\Delta = \tilde{Z}_{medium} - \tilde{Z}_{fine}$.

	Resistance			Reactance		
SPL	800 Hz	1400 Hz	2000 Hz	800 Hz	1400 Hz	2000 Hz
130 dB	0.029	0.042	0.044	0.054	0.090	0.146
150 dB	0.074	0.073	0.087	0.074	0.108	0.099

Table 2 Probe Position for Impedance Eduction Method.

	Probe 1	Probe 2	Probe 3	Probe 4	Probe 5	Probe 6	Probe 7	Probe 8
x position	−640 mm	−470 mm	−380 mm	−330 mm	330 mm	380 mm	470 mm	640 mm

B. Anechoic Terminations

Another important hypothesis is the non-reflection of acoustic waves in both duct terminations. This was verified by calculating the absorption coefficient of the terminations as seen by the first and last microphones in the model (measuring probes). The two-microphones technique was used to estimate the transfer function between probes 1 and 2 and between probes 7 and 8 (Table 2), an then the transfer function for the incident and reflected waves were calculated using the wavenumber of the tone and the space between the two microphones. Among all the six scenarios simulated, the smallest absorption coefficient was obtained for the 130 dB, 800 Hz case, with $\alpha = 98.2\%$.

V. Model Validation and Results

In the present study, a first attempt is made to simulate multiple cavities of a liner, what allows both impedance eduction and in-situ methods to be used to estimate the liner impedance. The following section presents the results obtained with both methods, and we analyze the results for different SPL and different cavities (in the case of the in-situ method) for the no flow case. The experimental data was obtained by Spillere et al. [13] in the UFSC liner test rig, for both the in-situ and eduction methods.

A. In-situ Results

The resistance and reactance components of the acoustic impedance obtained with the numerical in-situ method are shown in Fig. 5. This values were calculated using Eq. 10 for each of the eleven cavities and then averaged. Also shown in Fig. 5 are the experimental data obtained by Spillere et al. [13].

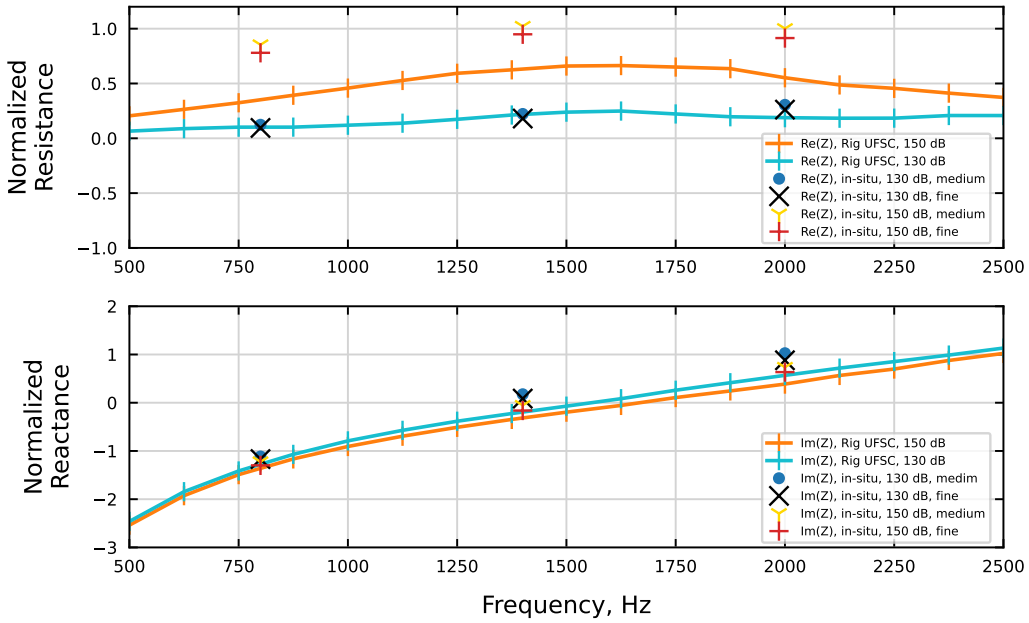

Fig. 5 In-situ measured data in the UFSC's rig and the numerical results obtained with the same method.

It can be seen from Fig. 5 that numerical and experimental impedances are in excellent agreement for sound pressure levels of about 130 dB. For higher SPLs, however, the simulated resistance is overestimated when compared to experimental results. Part of this is likely due to numerical discretization errors, since there are high pressure and

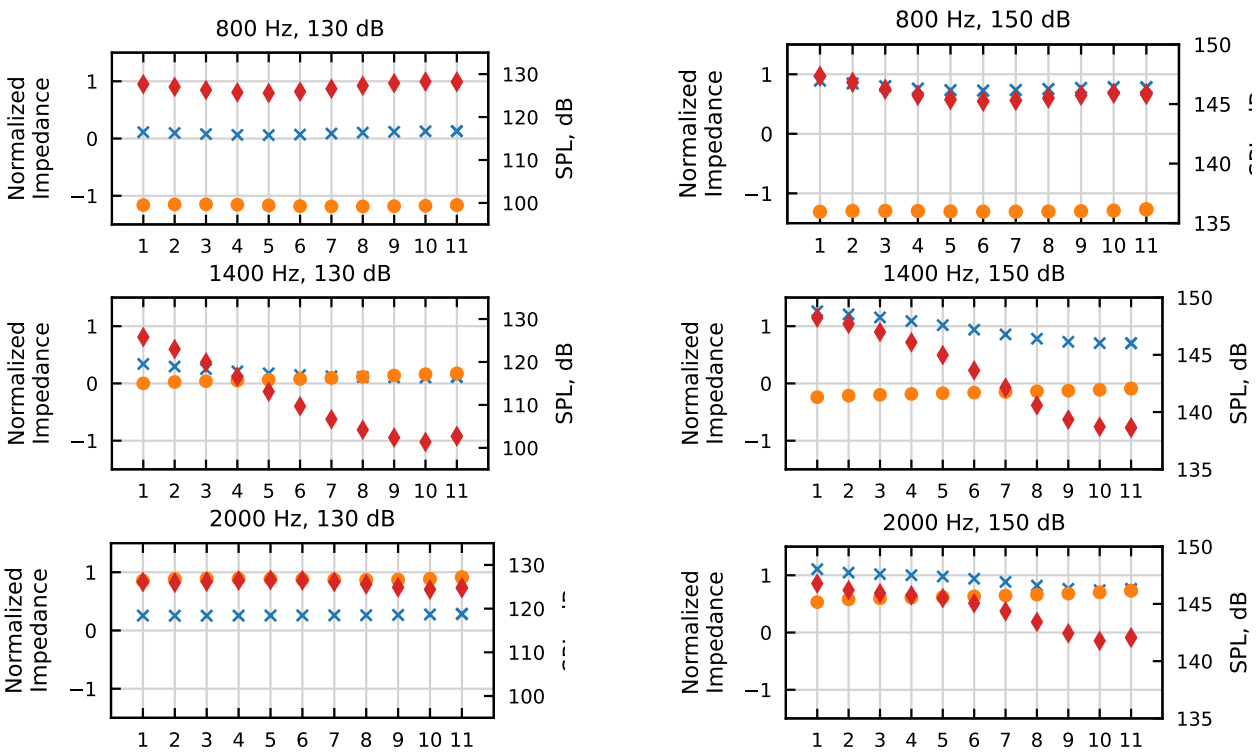

Fig. 6 Normalized impedance at each cavity calculated using Eq. 10: reactance (orange circle), resistance (blue x), and SPL (red diamond).

velocity gradients in the orifices region. This hypothesis is corroborated by the fact that the results for the the finer mesh tend to the experimental data. Another factor that could explain this larger differences for higher SPL is the shape of the orifices. The simulated orifices have perfectly sharp edges, which makes the *vena contracta* of the in and outflow smaller, and, therefore, the velocity gradient bigger, dissipating more energy due to viscous effects and increasing the liner's resistance, whereas the laser-cut orifices in the manufactured sample may have smoother edges. Nevertheless, the agreement observed between numerical and experimental data gives us confidence in the numerical model, and we may proceed to further analyze the results.

In the numerical model, its easy to probe every cavity simultaneously. Using Eq. 10, we calculated the impedance components for each cavity of the liner in the wave propagation direction, and the results are shown in Fig. 6, for the finer grid simulation for three frequencies and two SPLs. The left column presents the results for 130 dB excitation (at the source), whereas the right column presents the results for 150 dB, and each row corresponds to a source frequency. Fig. 6 shows the tendency of the liner's resistance to drop along its length, specially near its resonant frequency (around 1400 Hz), but also for higher frequencies. This tendency follows the drop in the sound pressure level, which is very sharp in the 1400 Hz frequency, as can be seen in the second row. For lower SPL in the succeeding cavity, the pressure and velocity gradients are smaller, which tends to dissipate less energy due to viscous effects, explaining the drop. It is also possible to observe a tendency of the liner's reactance to increase along its length, especially near its resonant frequency. As the SPL of the acoustic field drops along the liner's length, so do the velocity magnitude of the in and outflow in each orifice. For high SPL, non-linear phenomena are important, and the drop in SPL has an impact in the mass reactance of the liner [31]. When there is high sound pressure the particle displacement amplitude through the orifice may be high enough to the core mass in the orifice be mixed by the jet flow, loosing kinetic energy, and reducing the mass reactance [32]. So, when the SPL drops along the liner, it is expected that the reactance increases, and this is what we observe in the simulations.

B. Mode Matching Results

We shall now proceed to analyze the impedance eduction technique based on the mode matching method. For the no-flow case, the results are shown in Fig. 7, along the experimental results obtained by Spillere et al. [25]. Results for the 2000 Hz case have been left out due to some problems with the simulation. A few observations can be made from Fig. 7. For the low frequency case, the simulation underestimates the resistance educed when compared with the experimental data, while the numerical results overestimate the resistance educed in the resonant frequency. In the later case, mesh refinement bring the results to a better agreement. On the other side, below the liner resonance, the reactance for 130 dB and 150 dB are very similar, in line with the experimental results, but slightly above the value obtained in the experiments. Nevertheless, the simulated results captured the tendency of the high SPL reactance being slightly below the lower SPL at both frequency points analyzed, although the difference between experimental results being with the method uncertainty [11]. At the resonant frequency, the reactance is close to zero for the experimental results, as well as for the 130 dB simulated result. However, the simulated results for 150 dB are lower then expected, possibly due to the sharper edges of the hole in the simulation when compared to the manufactured samples as previously discussed. The fact that the simulation display a smaller number of cavities (11 cavities) than the sample used in the experimental analysis (17 cavities) may also help to explain the differences observed. The further drop in SPL in the longer sample may reduce the non-linear effects in the last cavities, increasing the reactance and lowering the resistance.

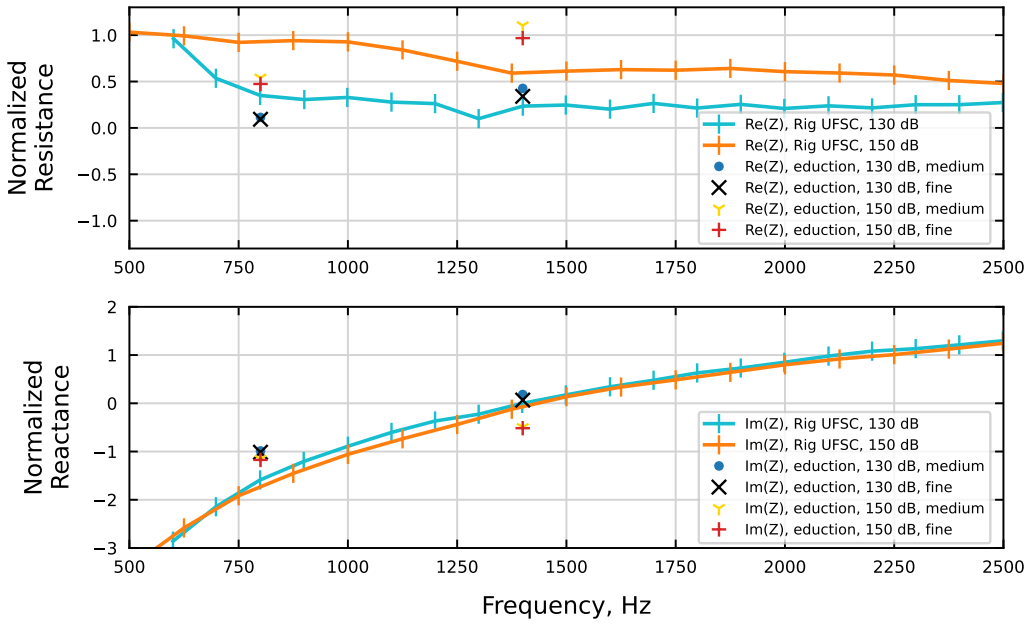

Fig. 7 Liner impedance educed from simulated and from experimental data.

C. In-situ and Eduction Comparison

In this section we will compare the impedance results obtained both numerically and experimentally using the two techniques. Fig. 8 shows this comparison for acoustic waves of 130 dB, whereas Fig. 9 shows it for 150 dB. It is interesting to note that both in-situ and educed impedances agree better in the simulated data than in the experimental data. In frequency ranges away from the liner resonance frequency, the acoustic field is less attenuated, and the uncertainties regarding the effective lined length and microphone positions may be relevant for the experimental impedance eduction technique [12]. On the other hand, in numerical simulations, the microphone positions and lined length are precisely known. In this way, the numerical liner impedance can be extracted irrespective of the method since they yield almost the same result. In addition, the numerical results at 800 Hz suggest that the experimental in-situ result is accurate, whereas at 1400 Hz and 2000 Hz the experimental eduction result is more likely to be correct.

Experimental uncertainty plays an important role in explaining the differences observed for the eduction results. As show by Bonomo et al. [11], experimental eduction methods suffer from high uncertainty in the low frequency region

of the impedance spectrum. The author used Monte Carlo Method to show that variability in the distance between microphones and in the sensitivity of each microphone may result in significant scattering in the results far from the resonant frequency of the liner. Zhou and Bodén [33] showed similar conclusions using a systematic multivariate uncertainty analysis technique. However, the numerical domain is much more precise in this regard, yielding results closer to the in-situ method, as this method is more precise in this region of the spectrum. A similar analysis is also presented by Spillere et al. [13], where the differences in impedances educed and calculated by in-situ is explored for experimental data in the context of a fan noise test rig.

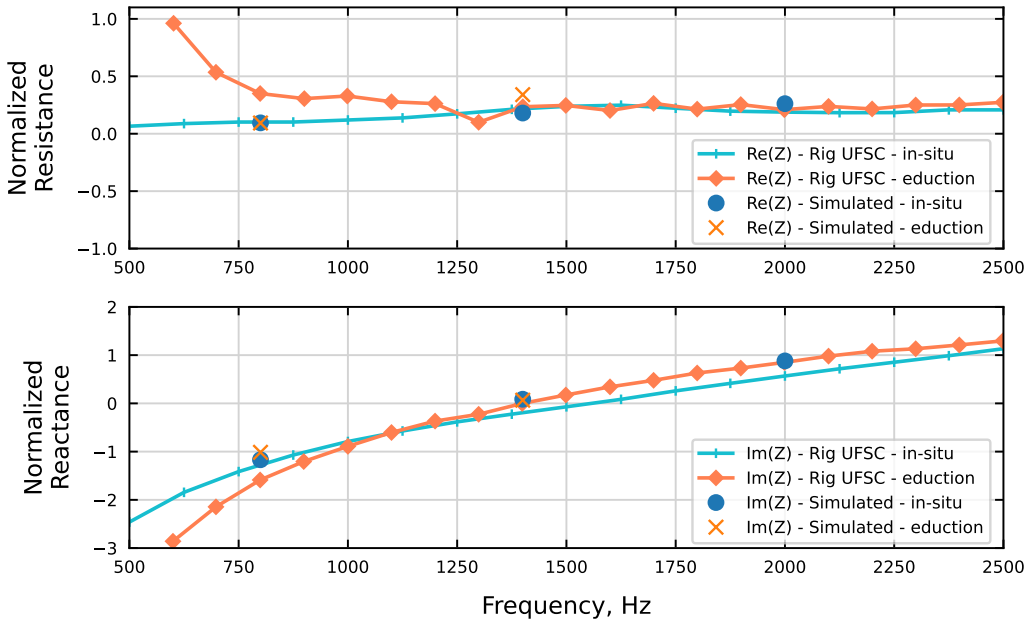

Fig. 8 Comparison between the impedance obtained with in-situ and impedance eduction methods, both for experimental and simulated results, and grazing acoustics waves of 130 dB**.**

D. Fluid Dynamic Field Analysis

The previous sections presented the impedance calculated in two different ways for a few scenarios. Fig. 6 showed the relation between cavity impedance and local SPL. We can now use the numerical results to better visualize some of the physics involved.

Fig. 10 shows the velocity magnitude for the orifices jet outflow phase, this is shown in the same acoustic wave phase, meaning each cavity is subjected to the same wavefront, but with different amplitudes, since the previous liner orifice has already attenuated it. This is useful for us to compare the strength of the outflow jets coming from withing each cavity, and it is evident that the jet gets smaller as the SPL drops along the liner. In the first cavity, the non-linear effects described by Westervelt [32] can be visualized when the hemispherical caps surrounding each orifice mass gets mixed by the jet flow, while for the eleventh cavity the orifice mass displacement is much smaller. Zhang and Bodony [34] showed that the discharge coefficient is closely related to the acoustic behavior of the liner. As the SPL drops along the liner, the discharge coefficient should increase, which is related to a smaller orifice boundary layer, yielding less resistance and more mass reactance, and this is exactly what we observe in Fig. 6.

Fig. 11 shows the simulated acoustic pressure field inside the duct at the resonant frequency, for a source of 150 dB. In the zoomed detail, we can see the wave front distortion, which highlights the presence of multiple modes in the lined section, which my be of important consideration for eduction techniques.

As show by Avallone et al. [7], the impedance measured using the in-situ technique is fairly sensitive to the measurement location. Fig. 12 shows the static pressure in the facesheet of the third cavity, where we can see a decreasing pressure gradient from left to right for a particular phase, bringing further evidence of the importance of probe location. Additionally, we can see a much more intense pressure gradient around each orifice, caused by the fluid

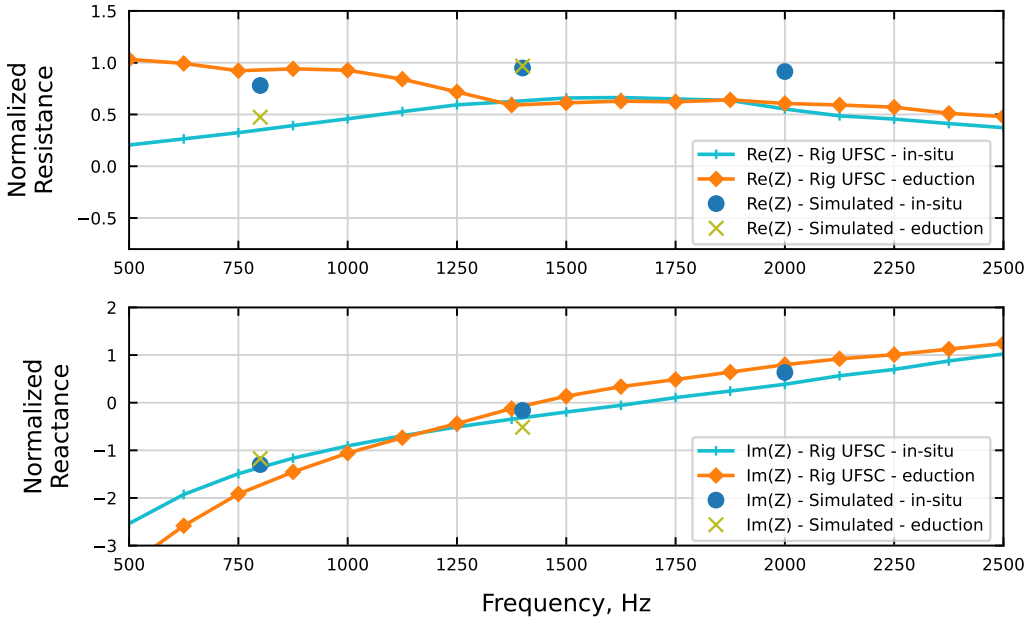

Fig. 9 Comparison between the impedance obtained with in-situ and impedance eduction methods, both for experimental and simulated results, and grazing acoustic waves of 150 dB**.**

ejection, particularly intense for high SPL. Fortunately, this gradient rapidly decreases to more characteristic pressure values, such that a probe located half a diameter outside the orifice's edge is already well representative of the intended measurement.

VI. Conclusions

This paper presented the results of a lattice-Boltzmann Very Large Eddy Simulation of an liner with eleven cavities mounted in a duct with the same configuration of the experimental rig at UFSC. This is the first time multiple cavities are simulated, allowing the eduction of the impedance from numerical data. Three frequencies and two SPL were simulated, totaling six data sets that were compared to experimental results obtained via mode matching by Spillere et al. [25] and via in-situ methods measured at UFSC for the purposes of this paper. Mesh convergence was used to verify the model's numerical errors, and termination absorbent coefficients were determined to verify the efficacy of the anechoic terminations. Boyh numerical in-situ and educed impedances were compared with experimental data sets to validate the model and verify its accuracy. As for the in-situ results, further analysis may be done to quantitatively assess the mass reactance increase with the drop in SPL along the lined section. Numerical data also allows for a deeper look into the effects of the measurement location, both in terms of the selected cavity and the microphone position within the cavity. A very import result was found when in-situ impedances were compared with educed ones. Both agree very well in the simulated results, but diverge in experimental results, specially in the low frequency range. Further investigation will be carried at UFSC's facilities. This paper represents a step towards the more complex numerical analysis of a lined duct with flow, and the use of different impedance measurement techniques. This step is necessary to set a solid basis to be build upon, mitigating uncertainties of various natures, such as mesh influence, non-linear behavior of the liner in high SPL and definition of a proper setup to implement impedance measurement techniques. For instance, from this milestone a setup to investigate the differences in educed impedance between upstream and downstream propagation can be carried on.

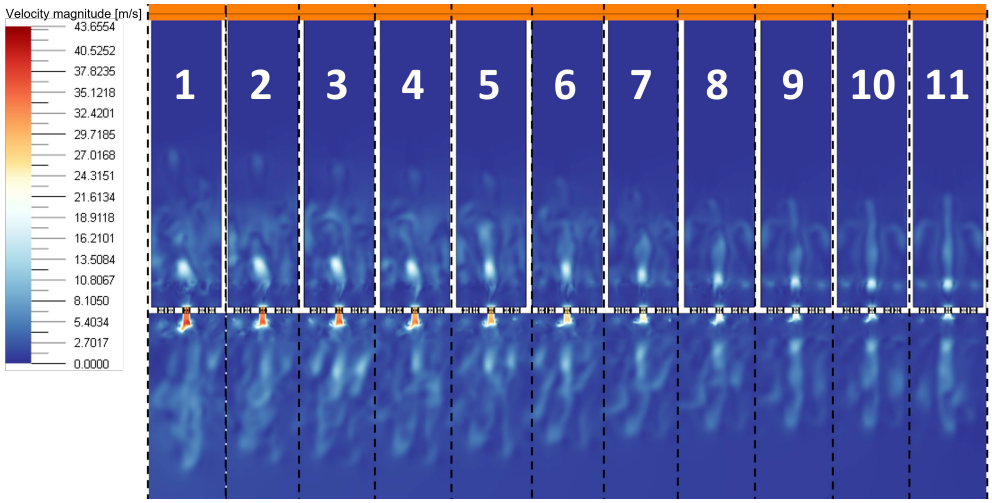

Fig. 10 Velocity magnitude for the outflow phase in each liner cavity at the same acoustic wave phase for f = 1400 Hz, SPL = 150 dB.

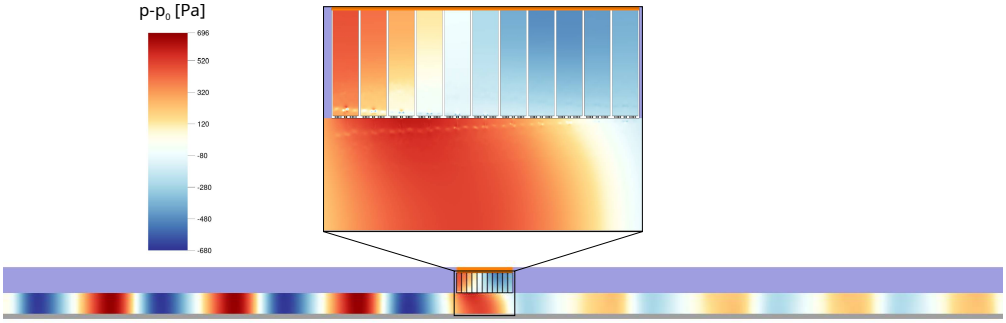

Fig. 11 Acoustic pressure field inside the duct for f = 1400 Hz and SPL = 150 dB.

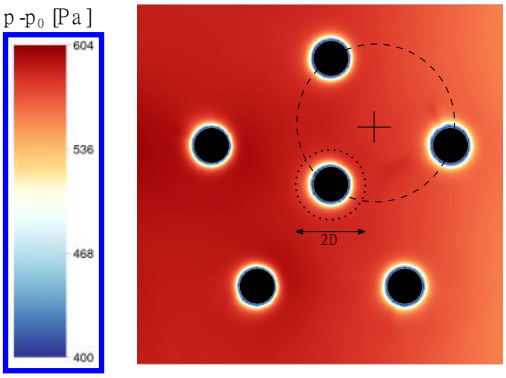

Fig. 12 Instantaneous static pressure distribution at the perforated plate below the third cavity (duct side), at the same instant of Fig.11. The centered cross shows the position of the in-situ probe.

Acknowledgments

L.S., A.S., L.B. and J.C. gratefully acknowledge the support from FINEP (Funding Authority for Studies and Projects), CNPq (National Council for Scientific and Technological Development) and EMBRAER S.A.

References

[1] Tam, C., Kurbatskii, K., Ahuja, K., and Gaeta, R., "A Numerical and Experimental Investigation of the Dissipation Mechanisms of Resonant Acoustic Liners," *Journal of Sound and Vibration*, Vol. 245, No. 3, 2001, pp. 545 – 557. https://doi.org/10.1006/jsvi.2001.3571.

[2] Tam, C., Ju, H., Jones, M., Watson, W., and Parrott, T., "A computational and experimental study of slit resonators," *Journal of Sound and Vibration*, Vol. 284, No. 3, 2005, pp. 947 – 984. https://doi.org/10.1016/j.jsv.2004.07.013.

[3] Tam, C. K., Ju, H., and Walker, B. E., "Numerical simulation of a slit resonator in a grazing flow under acoustic excitation," *Journal of Sound and Vibration*, Vol. 313, No. 3, 2008, pp. 449 – 471. https://doi.org/10.1016/j.jsv.2007.12.018.

[4] Zhang, Q., and Bodony, D. J., "Numerical Simulation of Two-Dimensional Acoustic Liners with High-Speed Grazing Flow," *AIAA Journal*, Vol. 49, No. 2, 2011, pp. 365–382. https://doi.org/10.2514/1.J050597.

[5] Tam, C. K., Ju, H., Jones, M., Watson, W., and Parrott, T., "A computational and experimental study of resonators in three dimensions," *Journal of Sound and Vibration*, Vol. 329, No. 24, 2010, pp. 5164 – 5193. https://doi.org/10.1016/j.jsv.2010.06.005.

[6] Zhang, Q., and Bodony, D. J., "Numerical investigation of a honeycomb liner grazed by laminar and turbulent boundary layers," *Journal of Fluid Mechanics*, Vol. 792, 2016, p. 936–980. https://doi.org/10.1017/jfm.2016.79.

[7] Avallone, F., Manjunath, P., Ragni, D., and Casalino, D., "Lattice-Boltzmann Very Large Eddy Simulation of a Multi-Orifice Acoustic Liner with Turbulent Grazing Flow," *25th AIAA/CEAS Aeroacoustics Conference*, American Institute of Aeronautics and Astronautics, Delft, The Netherlands, 2019. https://doi.org/10.2514/6.2019-2542, URL https://arc.aiaa.org/doi/10.2514/6.2019-2542, main.

[8] Dean, P., "An in situ method of wall acoustic impedance measurement in flow ducts," *Journal of Sound and Vibration*, Vol. 34, No. 1, 1974, pp. 97 – IN6. https://doi.org/10.1016/S0022-460X(74)80357-3.

[9] Jones, M., Watson, W., and Nark, D., "Effects of Flow Profile on Educed Acoustic Liner Impedance," *16th AIAA/CEAS Aeroacoustics Conference*, American Institute of Aeronautics and Astronautics, 2010. https://doi.org/10.2514/6.2010-3763, URL https://arc.aiaa.org/doi/10.2514/6.2010-3763.

[10] Tam, C. K., Pastouchenko, N. N., Jones, M. G., and Watson, W. R., "Experimental validation of numerical simulations for an acoustic liner in grazing flow: Self-noise and added drag," *Journal of Sound and Vibration*, Vol. 333, No. 13, 2014, pp. 2831 – 2854. https://doi.org/10.1016/j.jsv.2014.02.019.

[11] Bonomo, L. A., Spillere, A. M. N., and Cordioli, J. A., "Parametric Uncertainty Analysis for Impedance Eduction Based on Prony's Method," *AIAA Journal*, Vol. 58, No. 8, 2020, pp. 3625–3638. https://doi.org/10.2514/1.J059071, URL https://arc.aiaa.org/doi/10.2514/1.J059071, publisher: American Institute of Aeronautics and Astronautics.

[12] Spillere, A. M. N., Bonomo, L. A., Cordioli, J. A., and Brambley, E. J., "Experimentally testing impedance boundary conditions for acoustic liners with flow: Beyond upstream and downstream," *Journal of Sound and Vibration*, Vol. 489, 2020, p. 115676. https://doi.org/10.1016/j.jsv.2020.115676.

[13] Spillere, A. M. N., Braga, D. S., Seki, L. A., Bonomo, L. A., Cordioli, J. A., Rocamora Jr., B. M., Junior, P. C. G., and Reis, D. C. d., "Design of a single degree of freedom acoustic liner for a fan noise test rig," *International Journal of Aeroacoustics*, 2021. (Manuscript accepted for publication).

[14] Weng, C., Schulz, A., Ronneberger, D., Enghardt, L., and Bake, F., "Flow and Viscous Effects on Impedance Eduction," *AIAA Journal*, Vol. 56, No. 3, 2018, pp. 1118–1132. https://doi.org/10.2514/1.J055838.

[15] Chen, H., Chen, S., and Matthaeus, W. H., "Recovery of the Navier-Stokes equations using a lattice-gas Boltzmann method," *Phys. Rev. A*, Vol. 45, 1992, pp. R5339–R5342. https://doi.org/10.1103/PhysRevA.45.R5339.

[16] Mann, A., Perot, F., Kim, M.-S., and Casalino, D., "Characterization of Acoustic Liners Absorption using a Lattice-Boltzmann Method," *19th AIAA/CEAS Aeroacoustics Conference*, American Institute of Aeronautics and Astronautics, 2013. https://doi.org/10.2514/6.2013-2271, URL https://arc.aiaa.org/doi/10.2514/6.2013-2271.

[17] Krüger, T., Kusumaatmaja, H., Kuzmin, A., Shardt, O., Silva, G., and Viggen, E. M., *The Lattice Boltzmann Method: Principles and Practice*, Graduate Texts in Physics, Springer International Publishing, Cham, 2017. https://doi.org/10.1007/978-3-319-44649-3, URL http://link.springer.com/10.1007/978-3-319-44649-3.

[18] Shan, X., Yuan, X.-F., and Chen, H., "Kinetic theory representation of hydrodynamics: a way beyond the Navier–Stokes equation," *Journal of Fluid Mechanics*, Vol. 550, No. -1, 2006, p. 413. https://doi.org/10.1017/S0022112005008153, URL http://www.journals.cambridge.org/abstract_S0022112005008153.

[19] Bhatnagar, P. L., Gross, E. P., and Krook, M., "A Model for Collision Processes in Gases. I. Small Amplitude Processes in Charged and Neutral One-Component Systems," *Phys. Rev.*, Vol. 94, 1954, pp. 511–525. https://doi.org/10.1103/PhysRev.94.511.

[20] Chen, H., Zhang, R., and Gopalakrishnan, P., "Lattice Boltzmann Collision Operators Enforcing Isotropy and Galilean Invariance," , Jan. 2020. U.S. Patent US20200019662A1.

[21] Fares, E., "Unsteady flow simulation of the Ahmed reference body using a lattice Boltzmann approach," *Computers & Fluids*, Vol. 35, No. 8-9, 2006, pp. 940–950. https://doi.org/10.1016/j.compfluid.2005.04.011, URL https://linkinghub.elsevier.com/retrieve/pii/S0045793005001581.

[22] Chen, H., Filippova, O., Hoch, J., Molvig, K., Shock, R., Teixeira, C., and Zhang, R., "Grid refinement in lattice Boltzmann methods based on volumetric formulation," *Physica A: Statistical Mechanics and its Applications*, Vol. 362, No. 1, 2006, pp. 158–167. https://doi.org/10.1016/j.physa.2005.09.036, URL https://linkinghub.elsevier.com/retrieve/pii/S0378437105009696.

[23] Habibi, K., Gong, H., Najafi-Yazdi, A., and Mongeau, L., "Numerical Simulations of Sound radiated from Internal Mixing Nozzles with Forced Mixers using the Lattice Boltzmann Method," *19th AIAA/CEAS Aeroacoustics Conference*, 2013. https://doi.org/10.2514/6.2013-2143.

[24] Teixeira, C., "Incorporating Turbulence Models Into The Lattice-Boltzmann Method," *International Journal of Modern Physics*, Vol. 9, No. 8, 1998, pp. 1159–1175. URL http://adsabs.harvard.edu/abs/1998APS..DFD..FK04T, conference Name: APS Division of Fluid Dynamics Meeting Abstracts.

[25] Spillere, A., Braga, D. S., Seki, L., Bonomo, L. A., Cordioli, J. A., Martinez, B., Greco, P. C., Reis, D. C., and Coelho, E. L., "Inlet liner design for a fan noise test rig," *25th AIAA/CEAS Aeroacoustics Conference*, American Institute of Aeronautics and Astronautics, 2019. https://doi.org/10.2514/6.2019-2724, URL https://arc.aiaa.org/doi/10.2514/6.2019-2724.

[26] Ferrante, P., De Roeck, W., Desmet, W., and Magnino, N., "Back-to-back comparison of impedance measurement techniques applied to the characterization of aero-engine nacelle acoustic liners," *Applied Acoustics*, Vol. 105, 2016, pp. 129 – 142. https://doi.org/10.1016/j.apacoust.2015.12.004.

[27] Watson, W. R., and Jones, M. G., "A Comparative Study of Four Impedance Eduction Methodologies Using Several Test Liners," *19th AIAA/CEAS Aeroacoustics Conference*, American Institute of Aeronautics and Astronautics, Berlin, Germany, 2013. https://doi.org/10.2514/6.2013-2274, URL https://arc.aiaa.org/doi/10.2514/6.2013-2274.

[28] Jing, X., Peng, S., and Sun, X., "A straightforward method for wall impedance eduction in a flow duct," *The Journal of the Acoustical Society of America*, Vol. 124, No. 1, 2008, pp. 227–234. https://doi.org/10.1121/1.2932256.

[29] Levenberg, K., "A method for the solution of certain non-linear problems in least squares," *Quarterly of Applied Mathematics*, Vol. 2, No. 2, 1944, pp. 164–168. https://doi.org/10.1090/qam/10666.

[30] Marquardt, D. W., "An Algorithm for Least-Squares Estimation of Nonlinear Parameters," *Journal of the Society for Industrial and Applied Mathematics*, Vol. 11, No. 2, 1963, pp. 431–441. https://doi.org/10.1137/0111030.

[31] Melling, T., "The acoustic impendance of perforates at medium and high sound pressure levels," *Journal of Sound and Vibration*, Vol. 29, No. 1, 1973, pp. 1–65. https://doi.org/10.1016/S0022-460X(73)80125-7, URL https://linkinghub.elsevier.com/retrieve/pii/S0022460X73801257.

[32] Westervelt, P. J., "Acoustical Impedance in Terms of Energy Functions," *The Journal of the Acoustical Society of America*, Vol. 23, No. 3, 1951, pp. 347–348. https://doi.org/10.1121/1.1906770, URL http://asa.scitation.org/doi/10.1121/1.1906770.

[33] Zhou, L., and Bodén, H., "A systematic uncertainty analysis for liner impedance eduction technology," *Journal of Sound and Vibration*, Vol. 356, 2015, pp. 86–99. https://doi.org/10.1016/j.jsv.2015.07.001, URL https://linkinghub.elsevier.com/retrieve/pii/S0022460X1500574X.

[34] Zhang, Q., and Bodony, D., "Numerical investigation and modelling of acoustically excited flow through a circular orifice backed by a hexagonal cavity," *Journal of Fluid Mechanics*, Vol. 693, 2012, pp. 367–401. https://doi.org/10.1017/jfm.2011.537.